THE ART AND SCIENCE OF WIND TUNNEL WALL INTERFERENCE: NEW CHALLENGES

M. Mokry, M. Khalid, and Y. Mébarki
Institute for Aerospace Research
National Research Council Canada

Abstract

Several topics characterizing the current trends in wall interference research are discussed. The two-variable method, developed as an interactive-graphics desktop application, is demonstrated using the boundary pressure input from a subsonic wind tunnel. In the treatment of drag correction, a distinction is made between the wall-induced gradient effect and the change of tunnel-stream momentum. Based on a phenomenological description of transonic flow and CFD simulations, three different choking patterns are identified. Finally, PSP measurements of the boundary conditions of a transonic test section are discussed. The comparisons of pressure on the pressure-orifice tube and the surrounding portions of a perforated wall are believed to be the first of their kind reported.

Nomenclature

A	= test section boundary
C	= test section cross-sectional area
c	= chord length
C_D	= drag coefficient
C_p	= pressure coefficient
D	= drag force
F	= force
g	= gravitational acceleration
h	= test section height
M	= Mach number
m	= mass flux density
n	= outward unit normal to δV
p	= pressure
r	= distance
Re	= Reynolds number
Q	= wake cross-sectional area

S	= model reference area
t	= airfoil maximum thickness
U	= wind tunnel stream velocity
u	= non-dimensional velocity increment
V	= model volume
x	= axial coordinate
γ	= ratio of specific heats
Δ	= wall interference correction
ρ	= density
τ	= blockage parameter
ϕ	= perturbation velocity potential
Σ	= test section boundary

Subscripts

ch	= tunnel choking condition
e	= 'effective'
w	= wake
I	= wall interference
$0,1,2$	= upstream, model location, downstream
∞	= far upstream

1 Introduction

Wind tunnel wall interference is considered to be more of an engineering-approximation 'art' than a branch of exact aerodynamic 'science'. However, because wall interference is also a challenging and technically important subject, it has attracted the attention of many researchers since its foundation by Prandtl [1]. The topics selected for this paper are the interactive graphics programming techniques in subsonic wall interference, subsonic drag force corrections, applications of computational fluid dynamics (CFD) to transonic wall interference, and measurements of pressure distributions on perforated walls by the pressure-sensitive-paint (PSP) technology.

The renewed interest in subsonic wind tunnel interference is in part due to a recent controversy that there are two different pressure gradient corrections to the measured drag force [2]. We will establish that one of them indeed corrects for the pressure-gradient effect, while the other one will be used for the tunnel-stream momentum effect.

Transonic wall interference has been in the spotlight of active research for more than half a century. However, because of its strongly non-linear nature, the subject was almost intractable with the earlier solution methods. In the past few decades, substantial progress has been achieved through advances in computer technology and CFD methods.

The concluding part of the paper describes PSP measurements of pressure distributions on a portion of the perforated wall of a transonic test section. These comparisons of the pressure distributions on a measuring tube and the surrounding portions of the perforated wall are believed to be the first of their kind published.

2   Subsonic wall interference

Subsonic wall interference corrections based on idealized boundary conditions and linear theory have traditionally been available in textbooks or specialized manuals as simple formulae and work charts [3]. Recently, more elaborate procedures have been devised that use as input the measured test-section boundary data. In production wind tunnel testing, these new procedures are customarily integrated into the data reduction processes. However, for a real-time data analysis, a better alternative offers interactive-graphics wall interference packages running on workstations or personal computers.

An example of a desktop application developed with Visual C++ for half-model testing in a solid-wall, rectangular test section has recently been described by Mokry [4]. The application implements the two-variable correction method of Ashill [5][6]. In this method, the wall-interference velocity potential ϕ_I is assumed to be harmonic inside the test section and evaluated according to the Green's theorem as

$$\phi_I = \frac{1}{4\pi} \iint_{\Sigma} \left[\frac{\partial \phi}{\partial n} \frac{1}{r} - \phi \frac{\partial}{\partial n} \left(\frac{1}{r} \right) \right] d\Sigma \qquad (1)$$

Here, Σ is the test section boundary, n is its outward normal, and r is the distance between the interior observation point and the point on the surface element $d\Sigma$. The normal derivative $\partial \phi / \partial n$ is the measured normal velocity component (zero for solid walls) and ϕ is the surface value of the perturbation velocity potential, obtained by integrating the measured axial component of perturbation velocity. The direct contribution of the model drops out of integral (1) because its velocity potential is harmonic in the (fictitious) tunnel exterior, not interior. The numerical evaluation of Eq.(1) is implemented by dividing the walls into constant-density source and doublet panels.

The flat-plate test data [7], recently obtained in the IAR 0.9m x 0.9m Low Speed Wind Tunnel, is used here as an example. The boundary pressure was measured by 240 orifices in total, distributed along 5 rows of orifices in each of the port, top, and starboard walls. An unfolded view of the walls with orifices and measured pressure coefficients, indicated by colors and streamwise profiles, are shown Fig.1a. The pressure coefficients in the upstream and downstream computational panels were obtained by interpolation. The floor, not shown in Fig.1, is considered as a plane of symmetry.

The corresponding surface distribution of

$$\phi = -\tfrac{1}{2} \int C_p \, dx$$

is shown in Fig.1b. The normal velocity, $\partial \phi / \partial n$, is not plotted because it is assumed zero everywhere on the boundary except at the exit plane, where it is set equal to $-C_p/2$.

The obtained correction $\partial \phi_I / \partial x$ to the axial component of velocity in the ground plane is shown in Fig.2. The thick vertical line segment indicates the location and size of the flat-plate model.
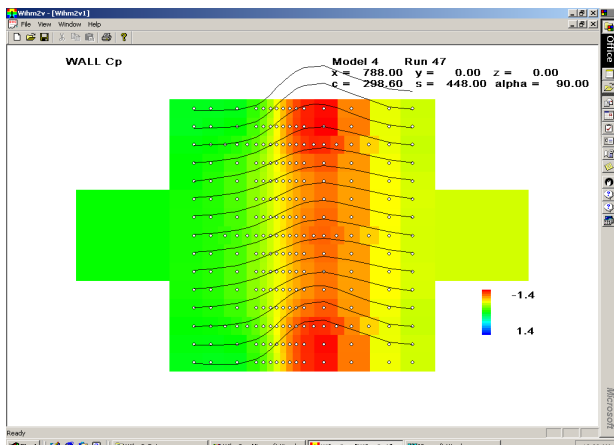
a) pressure coefficient, *Cp*
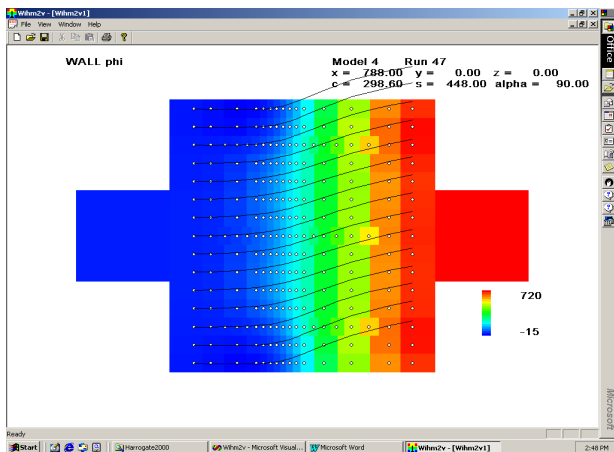
b) perturbation velocity potential, ϕ

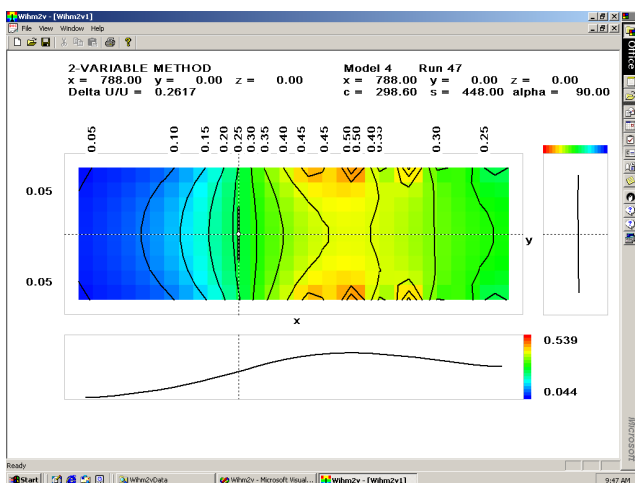**Fig.1   Wall data for a flat-plate test**

Fig.2 Axial velocity correction for a flat-plate test.

The interference velocity profile in the bottom portion of Fig.2 displays a difference in upstream and downstream levels and a gradient at the model location, which are the prominent features of wake blockage. The presence of solid blockage is also detectable: the axial component of wall interference does not attain its maximum far downstream, but at a finite distance downstream of the model.

The menu/dialog driven software is capable of displaying all three components of wall interference velocity in the horizontal, vertical and cross-flow planes.

3   Wall-induced drag

The distributions of wall interference velocity provide a detailed diagnosis of the flow environment of the tested model. As discussed in Ref.[8], an important practical task is to translate this information into model force corrections.

We shall analyze two types of blockage corrections to the measured drag force: the static and dynamic one. Currently, the correction proportional to the product of model volume and drag as well as the correction proportional to the square of drag are recognized, but the clear distinction is seldom made [2], [9].

3.1 Static correction

This drag force correction [3] is evaluated according to the laws of hydrostatics. Using Gauss' theorem, the integral of pressure over the surface of the body is converted into the integral of the pressure gradient

$$\vec{F} = -\iiint_V \nabla p \, dV \qquad (2)$$

over the volume *V* of the body. If the ambient pressure gradient is constant, then the buoyancy force is given by:

$$\vec{F} = -V \nabla p \qquad (3)$$

The familiar law of Archimedes is obtained from Eq.(3) by substituting $-\rho g$ for the vertical component of ∇p. In a wind tunnel, the forces of gravity do not play a significant role, but

there is a wall-induced pressure gradient in the wind tunnel stream. From the Bernoulli equation, it follows that for a small increment of stream static pressure

$$\Delta p = -\rho\, U\, \Delta U = -\rho\, U^2 u$$

where

$$u = \Delta U / U$$

is the non-dimensional increment of stream velocity. The drag force correction ΔD, defined as equal and opposite to the streamwise component of buoyancy force, is according to Eq.(3)

$$\Delta D \equiv -F_x = -V_e \rho\, U^2 \left.\frac{\partial u}{\partial x}\right|_1 \qquad (4)$$

where subscript 1 indicates the model position, Fig.3. The fact that the air around the model is not stationary is accounted for by replacing the actual model volume V by an 'effective' volume V_e. As discussed in [3], V_e depends on the shape of the body and, as a rule, $V_e > V$ if $\partial u/\partial x > 0$.

In terms of the drag coefficient

$$C_D = \frac{2D}{\rho\, U^2 S}$$

the buoyancy correction is

$$\Delta C_D = -2\frac{V_e}{S}\left.\frac{\partial u}{\partial x}\right|_1 \qquad (5)$$

where S is the model reference area. In a solid-wall wind tunnel the velocity derivative is proportional to wake drag, so that in this case
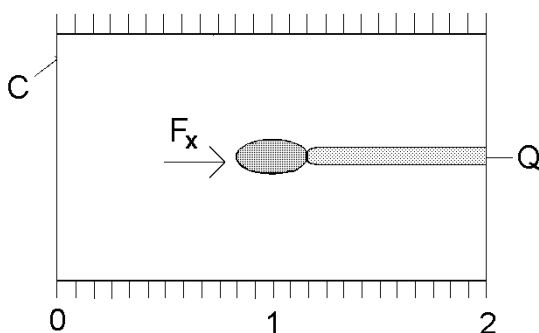
$$\Delta C_D \propto -C_D V_e$$

Fig.3   Illustrating wake blockage.

A common practice is to evaluate the drag correction from the empty-tunnel gradient, but of course a more rigorous approach is to use that induced by the walls in the presence of the model. Nevertheless, in the flat-plate case, shown in Fig.2, the buoyancy drag correction would be zero, because the plate has a negligible volume.

3.2 Dynamic correction

The dynamic correction to the measured drag can be obtained from the balance of the axial momentum. We denote, according to Fig.3, by C and Q the cross-sectional areas of the test section and wake respectively. The conservation of mass, energy and momentum between station 0 far upstream and station 2 far downstream is described by

$$CU_0 = (C - Q)U_2 \qquad (6)$$

$$\tfrac{1}{2}\rho\, U_0^2 + p_0 = \tfrac{1}{2}\rho\, U_2^2 + p_2 \qquad (7)$$

$$C\left(\rho\, U_0^2 + p_0\right) = \qquad (8)$$
$$(C - Q)\left(\rho\, U_2^2 + p_2\right) + Q p_w + F_x$$

where p_w is pressure across the wake and F_x is the axial force acting on the model. Assuming $p_w = p_2$, it follows from Eqs.(6)-(8) that

$$\Delta D \equiv -F_x = -\tfrac{1}{2}\rho\, U_0^2 C (U_2/U_0 - 1)^2 \qquad (9)$$

The corresponding drag coefficient correction is

$$\Delta C_D = -(C/S)u_2^2 \qquad (10)$$

where

$$u_2 = (U_2 - U_0)/U_0 \qquad (11)$$

is the non-dimensional velocity increment far downstream of the model.

Since the viscous drag can be approximated as $D \approx Q\rho U_2{}^2$, it follows from Eqs.(6) and (11)

$$u_2 \approx \tfrac{1}{2}C_D\, S/C$$

and from Eq.(10)

$$\Delta C_D \approx -\tfrac{1}{4} C_D^2 \, S / C \qquad\qquad (12)$$

Equations (10) and (12) contain neither the model volume nor the local velocity gradient and hence do not correct for the buoyancy effect. They correct for the (incremental) tunnel stream momentum effect, but of course only in the solid-wall test sections because in their derivation we have not accounted for the mass and momentum fluxes through the walls.

4   Transonic wall interference

Transonic wall interference has eluded a rational evaluation for some time, mainly because of the lack of understanding of the non-linear flow phenomena. The first effort to calculate a weakly supercritical flow past a NACA 0012 airfoil in a wind tunnel and free air, was made by Emmons [10]. Elaborate relaxation calculations, conducted by his colleagues, would not converge for higher stream Mach numbers. Only relatively recently has a substantial progress been enabled by the advances in computer technology and CFD methods. However, a coherent methodology of transonic wall interference assessment is still lacking. Before discussing the subject in greater detail, we shall review three basic free-stream patterns of transonic flow.

The supercritical flow shown in Fig.4a retains the essential features of subsonic flow: a perturbation which occurs at an arbitrary location influences the entire flow field, although the mechanism of propagation is different in the infinite subsonic and finite supersonic regions [11]. If the supersonic 'pocket' does not reach the walls, it may be possible to relate the wind tunnel measurement to free-air flow by correcting the wind tunnel Mach number and geometrical incidence, as in subsonic flow.

As the free stream Mach number increases, the supersonic flow region grows in size and the closing shock wave moves toward the trailing edge. At $M_\infty = 1$ the flow pattern changes qualitatively as the supersonic region also becomes infinite. As illustrated in Fig.4b, the

sonic line extends from the point S on the profile to infinity and so does the tail shock wave, originating at the trailing edge point T. Among the family of characteristics of special significance is the 'limiting' one, which extends from the surface point L and approaches the sonic line asymptotically. This limiting characteristic divides the supersonic region into two parts: one, in which the characteristics originating on the surface reflect from the sonic line and the other where this is not the case. Airfoil perturbations emanating between S and L influence the subsonic flow region; those emanating between L and T do not.
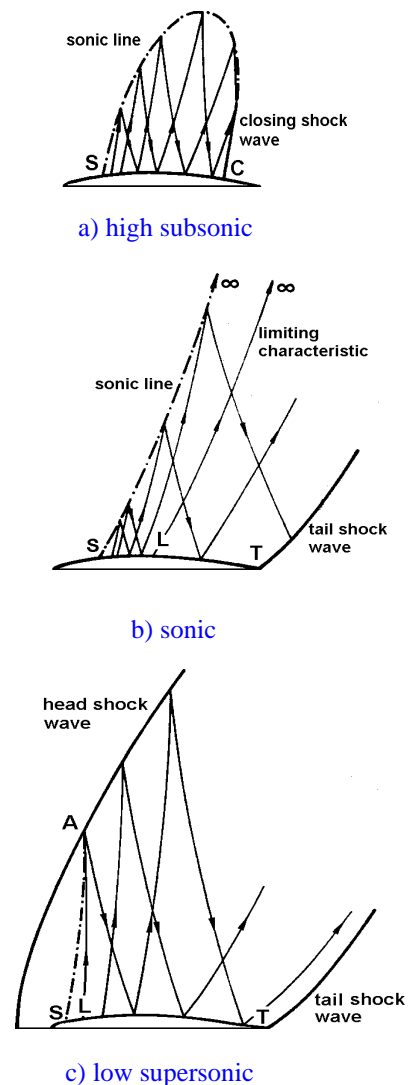

a) high subsonic

b) sonic

c) low supersonic

Fig.4   Transonic flow past an isolated airfoil (after Dvořák [11]).

For an airfoil between wind tunnel walls, the limiting characteristic is the one passing through the intercept A of the sonic line and the wall, as illustrated Fig.5. The characteristics that originate upstream of point L reach the sonic line and reflect in much the same manner as in the case of unbounded flow. However, those that originate downstream of L do not propagate outward indefinitely, but reflect from the wind tunnel wall [12]. This wave-reflection interference is similar to that occurring at supersonic speeds. An important difference is that, in a solid-wall wind tunnel, this situation occurs well before M_∞ reaches unity, at the choked-flow condition.
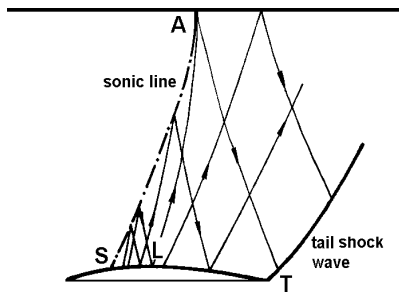
Fig.5 Choked flow past an isolated airfoil.

For supersonic stream, $M_\infty > 1$, the subsonic region reduces to a finite size, confined between the head shock wave and the sonic line, Fig.4c. Similar to the previous case, a limiting characteristic exists here, dividing the supersonic portion of the airfoil surface into two parts: one that influences the subsonic region and the other one that does not. Testing in a solid-wall wind tunnel is possible only if M_∞ is considerably larger than unity, so that the head shock wave reduces flow velocity to that below the subsonic choking Mach number.

Because, near sonic conditions, flow perturbations propagate primarily in the direction normal to flow, a fair estimate of the choking interval can be obtained from one-dimensional stream tube theory. We assume that h is a constant test section height and t the maximum thickness of the tested airfoil. The numbering of the stations is the same as in Fig.3. Conservation of mass between the upstream station 0 and the airfoil station 1 gives

$$h\rho_0 U_0 = (h-t)\rho_1 U_1 + 2\int_{x_0}^{x_1} \rho\, V dx \qquad (13)$$

where V is the normal velocity through the (single) wall. Introducing the mass flux density ratio

$$m = \frac{\rho V}{\rho_0 U_0} \qquad (14)$$

we obtain

$$1 - \tau = \frac{\rho_0 U_0}{\rho_1 U_1} \qquad (15)$$

where

$$\tau = \left(t - 2\int_{x_0}^{x_1} m\, dx \right) \Big/ \left(h - 2\int_{x_0}^{x_1} m\, dx \right) \qquad (16)$$

If $m=0$, then τ is simply the blockage ratio t/h. For isentropic flow, it follows from Eq.(15) that

$$1 - \tau = \frac{M_0}{M_1}\left[\frac{2 + (\gamma-1)M_1^2}{2 + (\gamma-1)M_0^2} \right]^{\frac{\gamma+1}{2(\gamma-1)}} \qquad (17)$$

where $\gamma = 1.4$ for air. Setting $M_1 = 1$ and $M_0 = M_{ch}$, we obtain for the choking Mach number

$$\tau = 1 - M_{ch}\left[1 + \tfrac{1}{6}(M_{ch}^2 - 1) \right]^{-3} \qquad (18)$$

The dependence of τ on M_{ch} described by Eq.(18), is the Allen-Vincenti parabola [13]. As illustrated in Fig.6, for any $\tau > 0$ Eq.(18) has two roots: $1 > M_{ch}^{(1)} > 0$ and $1 < M_{ch}^{(2)}$, which determine the subsonic and supersonic limits of the choking interval, respectively. No tunnel stream Mach number M_0 can be established between these limits. As illustrated in Fig.6, for the NACA 0012 profile having $t/c = 0.12$ and a solid-wall test section providing $h/c = 5$, we have $\tau = t/h = 0.024$ (dashed line). The choking Mach numbers, evaluated from Eq.(16) by Newton's method, are $M_{ch}^{(1)} = 0.837$ and $M_{ch}^{(2)} = 1.179$.
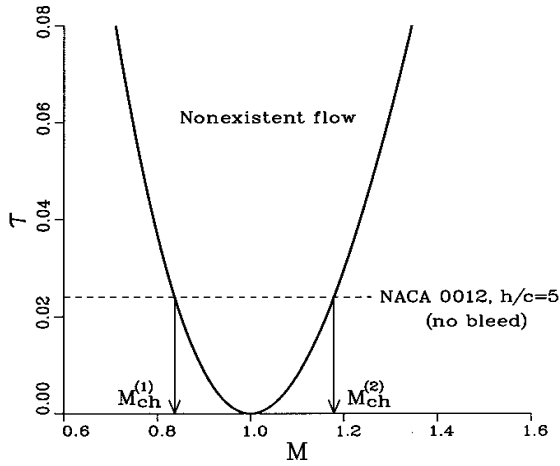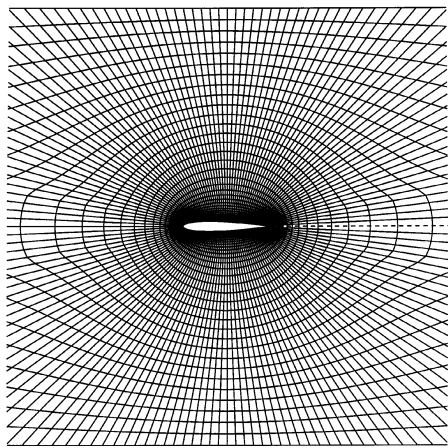
Fig.6 Choking interval in one-dimensional flow.

a) central portion

b) entire (smaller scale)

Fig.7   Computational mesh.

The single-block, wind tunnel mesh [14], used to verify the choking interval with the inviscid-flow (Euler) version of the NPARC code [15] is shown in Fig.7. A 'free stream' Mach number M_∞ was imposed at the circular front end of the mesh and a solid-wall, slip boundary condition was applied both on the NACA 0012 airfoil contour and the parallel wind tunnel walls.
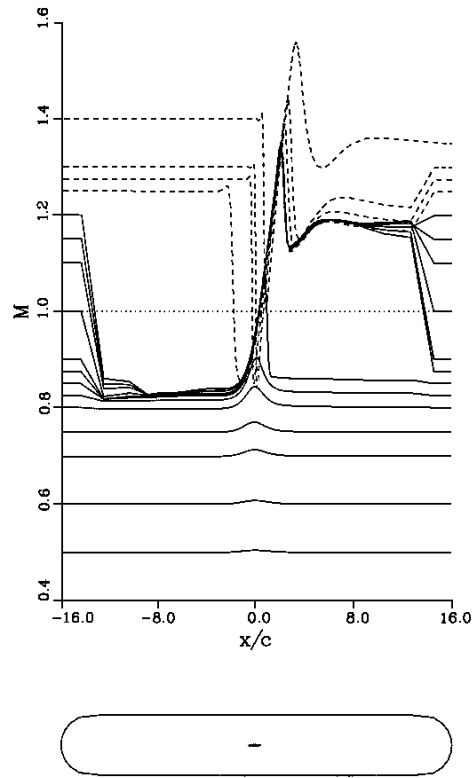

Fig.8   Wall Mach number for NACA 0012 in solid wall test section, h/c=5.

Computed wall Mach number distributions are plotted in Fig.8 for a sequence of selected M_∞. It is seen that for $M_\infty \leq M_{ch}^{(1)}$ the value

$$M\big|_{x/c=-16} = M_\infty$$

is retained as the true tunnel Mach number upstream and downstream of the airfoil. On the choking interval $M_{ch}^{(1)} \leq M_\infty \leq M_{ch}^{(2)}$ the code overrides the specified M_∞ by invoking a compression in the first upstream layer of mesh cells. As may be verified on the dash-line profiles, the values of $M_\infty \geq M_{ch}^{(2)}$ are again accepted as tunnel Mach numbers but, due to the entropy increase, accurately enough only upstream of the airfoil. In effect, the CFD virtual wind tunnel behaves very much like a real one.
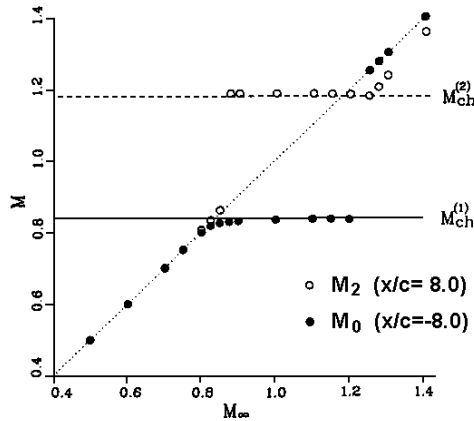
Fig.9 Mach numbers upstream and downstream of the airfoil as functions of M_∞ specified at the upstream end of the mesh.

Figure 9 shows a plot of the wall Mach numbers M_0 and M_2 evaluated halfway between the airfoil and the upstream and downstream ends of the wind tunnel. The observations can be generalized as follows:

(i) $M_0 = M_2 = M_\infty$ for $M_\infty < M_{ch}^{(1)}$

(ii) $M_0 = M_{ch}^{(1)}$, $M_2 = M_{ch}^{(2)}$ for $M_{ch}^{(1)} < M_\infty < M_{ch}^{(2)}$

(iii) $M_0 = M_\infty$, $M_{ch}^{(2)} < M_2 < M_\infty$ for $M_\infty > M_{ch}^{(2)}$.

Clearly, the one-dimensional prediction of the choking interval $[M_{ch}^{(1)}, M_{ch}^{(2)}]$ from Eq.(18) is very satisfactory.

From Fig.9 it is also apparent that there are three inviscid-flow choking patterns [16]. The fourth, providing the passage from supersonic to subsonic flow, is unstable [17]. The Mach contours of the three possible patterns, obtained by NPARC, are shown in Fig.10. In cases a) and b) the same location of the sonic line and identical Mach distributions on the airfoil surface are obtained.

Case c) is not vastly different because the head shock wave reduces the supersonic $M_{ch}^{(2)}$ to the subsonic $M_{ch}^{(1)}$ if the former is sufficiently close to unity. The proof of this not- so-obvious assertion can be given as follows. By differentiating the relationship between the Mach numbers downstream and upstream of a normal shock wave
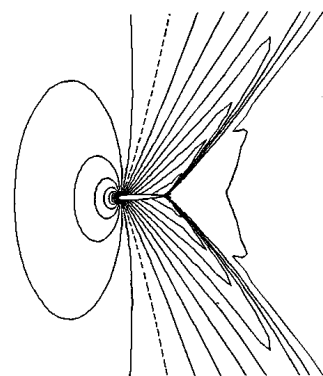
$$\overline{M}_0^2 = \frac{2 + (\gamma - 1)M_0^2}{2\gamma M_0^2 - (\gamma - 1)}, \quad M_0 \geq 1$$

we obtain
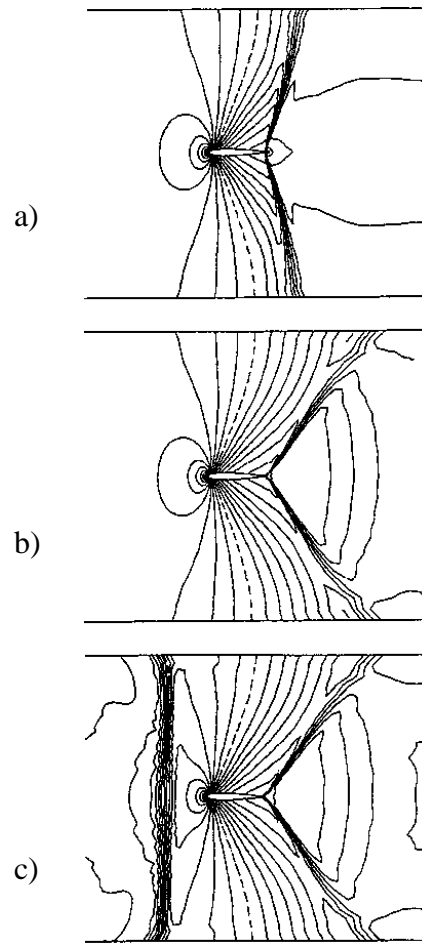
Fig.10 Choked-flow isomach patterns for a NACA 0012 in test section with solid walls:

a) subsonic-subsonic, $M_0 = M_{ch}^{(1)}$, $M_2 = M_{ch}^{(1)}$

b) subsonic-supersonic, $M_0 = M_{ch}^{(1)}$, $M_2 = M_{ch}^{(2)}$

c) supersonic-supersonic, $M_0 = M_{ch}^{(2)}$, $M_2 = M_{ch}^{(2)}$

Fig. 11 Isomachs for sonic flow around a NACA 0012.

$$d\overline{M}_0 = -dM_0, \quad M_0 = 1$$

Accordingly, the Mach numbers after and before the shock wave deviate from unity by equal amounts and by opposite signs (sonic freeze principle). The symmetry of the choking interval at $M_0 = 1$ is verified by substituting, $M_{ch}=1+\varepsilon$, $|\varepsilon| << 1$ in Eq.(18) and expanding the term in square brackets in a binomial series. To the lowest order of approximation, $\tau = (5/6)\varepsilon^2$. Therefore, if $M_0 = M_{ch}^{(2)} = 1 + \sqrt{(6\tau/5)}$, then $\overline{M}_0 = M_{ch}^{(1)} = 1 - \sqrt{(6\tau/5)}$, which completes the proof.

The principal difference in the choking patterns of Fig.10 is in the slope of the tail shock wave. Existence of both the *strong shock* with the downstream state subsonic, Fig.10a, and the *weak shock* with the downstream state supersonic, Figs.10b and 10c, can be verified on the hodograph shock polar [17]. Wind tunnel experiments [18] indicate that in the presence of the wall boundary layer, the slope of the actual tail shock wave can be anywhere between the two inviscid-flow slopes, depending on the back pressure.

The subsonic-supersonic choking flow, case b), is similar to the corresponding portion of free-air flow at $M_\infty = 1$ past the same airfoil, Fig.11. Nevertheless, the surface Mach numbers for these two flow conditions differ quite a bit, Fig.12. The difference cannot be bridged by a global Mach number correction because in the wind tunnel case the surface M no longer increases once choking occurs, and in the free air case M is frozen at $M_\infty = 1$:

$$dM / dM_\infty = 0, \quad M_\infty = 1$$

A substantial decrease of M_∞ would be required to reduce the surface M obtained in free air to that obtained at the same location in the wind tunnel. However, when this occurs, the free-air flow pattern has already changed from the sonic, Fig.4b, to the high subsonic, Fig.4a. In the example of Fig.12, the free-air distribution computed at $M_\infty = 0.85$ agrees well with that for the choked wind tunnel, but only upstream of the closing shock wave.
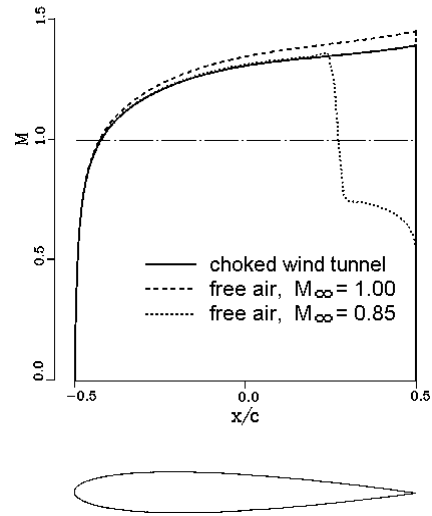

Fig.12 Surface Mach number for a NACA 0012

The simulation of flow with free-stream Mach number one in a choked wind tunnel is by no means a new idea. It has been studied both experimentally and theoretically in the 1950s, most notably by Spreiter et al [12]. Among the factors found to affect the simulation are the model thickness ratio, influencing the wave-reflection type of interference, and size of the test section with respect to the model. In general, the reduction of the blockage parameter τ narrows the choking interval, see Fig.6. For a satisfactory quantitative agreement of the wind tunnel and free-air Mach distributions, the choking interval should only be as wide as the transonic freeze interval [16]. This condition is practically impossible to achieve in a solid-wall test section unless, of course, the walls can be flexed. The most effective reduction of τ can be realized by venting air into the plenum, as approximated by Eq.(16). In transonic wind tunnels with ventilated test section walls, it is in principle possible to increase M_0 continuously to and through Mach one without choking [19]. Unfortunately, we do not have yet a sufficient knowledge of the cross-flow properties of ventilated walls to be able to evaluate their interference effects reliably.

5 PSP measurements of wall boundary conditions

Measurements of the boundary condition at perforated walls present a difficult technical problem [20], because the normal velocity is dependent not only on the pressure difference across the wall, but also on the ambient pressure gradient and wall boundary layer [21]. However, contemporary measurement techniques such as PSP permit investigating flow near the wall in all its complexity. It is possible to quantify the flow inhomogeneities near the perforations and relate the pressure distribution on the wall to the discrete pressure tap readings on the measuring devices such as static pressure tubes or rails.

This exploratory PSP test was performed as an addendum to the half-model experimental program [22] in the IAR 1.5m x 1.5m Blowdown Wind Tunnel. Towards this goal, a rectangular area of 0.26m x 0.18m of the perforated floor, shown in Fig.14, was sprayed with the ISSI Pt(TfPP)-based Uni-Coat. By pitching the half model, different flow conditions at the wall could be produced.

The PSP patch, covering a portion of a pressure-measuring tube, is shown in detail in Fig.15. Halogen lamps, filtered to provide a green-light broadband around 525 nm, were used to excite the paint. A Photometric CCD camera, equipped with a filter selected to transmit the red-light luminescence near 650 nm, was used to acquire the images. The camera output was digitized at 1024 x 1024 pixel resolution. Image data processing was performed on a personal computer.

A painted coupon was calibrated in a dedicated calibration chamber for the dependence of the emitted light intensity on pressure and temperature. The two pressure taps available on the painted portion of the tube were used to align the wind-off and wind-on images (to compensate for camera motion) and to account for temperature effect (assuming constant temperature over the patch).
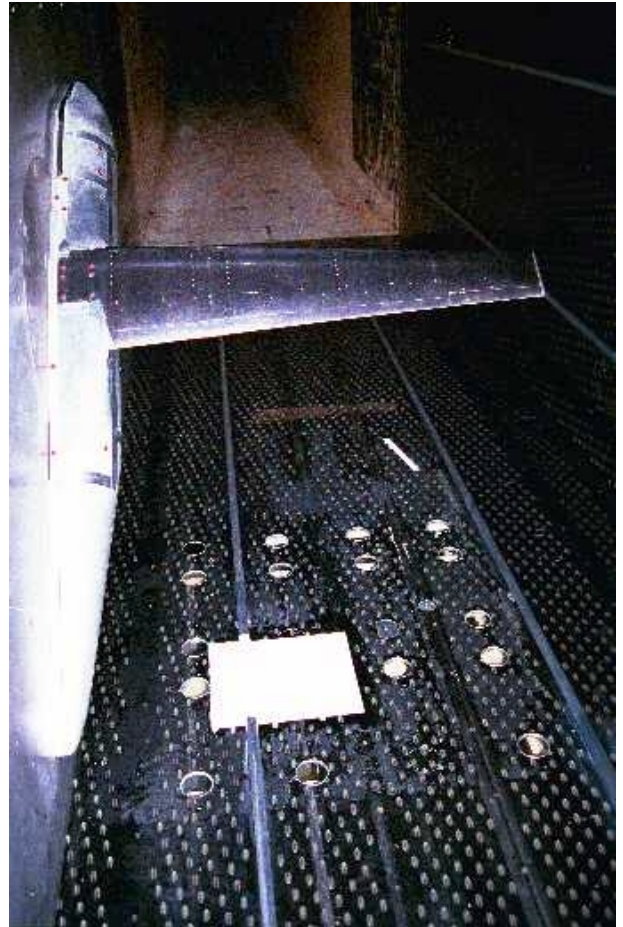
**Fig.14 PSP patch on the bottom wall of the IAR 1.5m x 1.5m High Speed Wind Tunnel.**
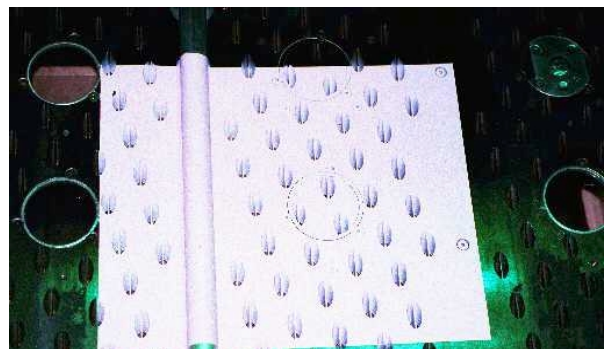
Fig.15 Detail of the PSP patch (optical window replaced by a perforated-wall insert).

Examples of the PSP-measured wall pressure coefficients at $Re=42\times10^6$ (based on a wall reference length of 1 meter), $M_\infty=0.74$ and three angles of attack are shown in Fig.15. In this figure, the x-coordinate is normalized by $c=25.4$ mm (data-reduction default value), with the origin at the rotation center of the half-model balance. Of the three cases shown, the best agreement of C_p measured along the pressure tube (Station 1) and line between the perforations (Station 2) is found for model angle of attack $\alpha=5^{\circ}$. In this case $C_p>0$ over most of the PSP patch and local outflow from the test section into the plenum is likely to be the case. The poorest agreement is found for $\alpha=-5^{\circ}$, in which case $C_p<0$ over the patch and local inflow into the test section takes place.

One may ask if this information is of any use in practical wall interference evaluation. Probably not at the moment because only a very incomplete picture has been obtained so far: the knowledge of C_p over the open portions of the walls (perforations) and normal component of velocity is absent. However, there may be other experimental techniques well suited to providing the missing information. The current PSP observation is considered as a first step towards a more realistic assessment of wind tunnel interference in perforated-wall test sections.
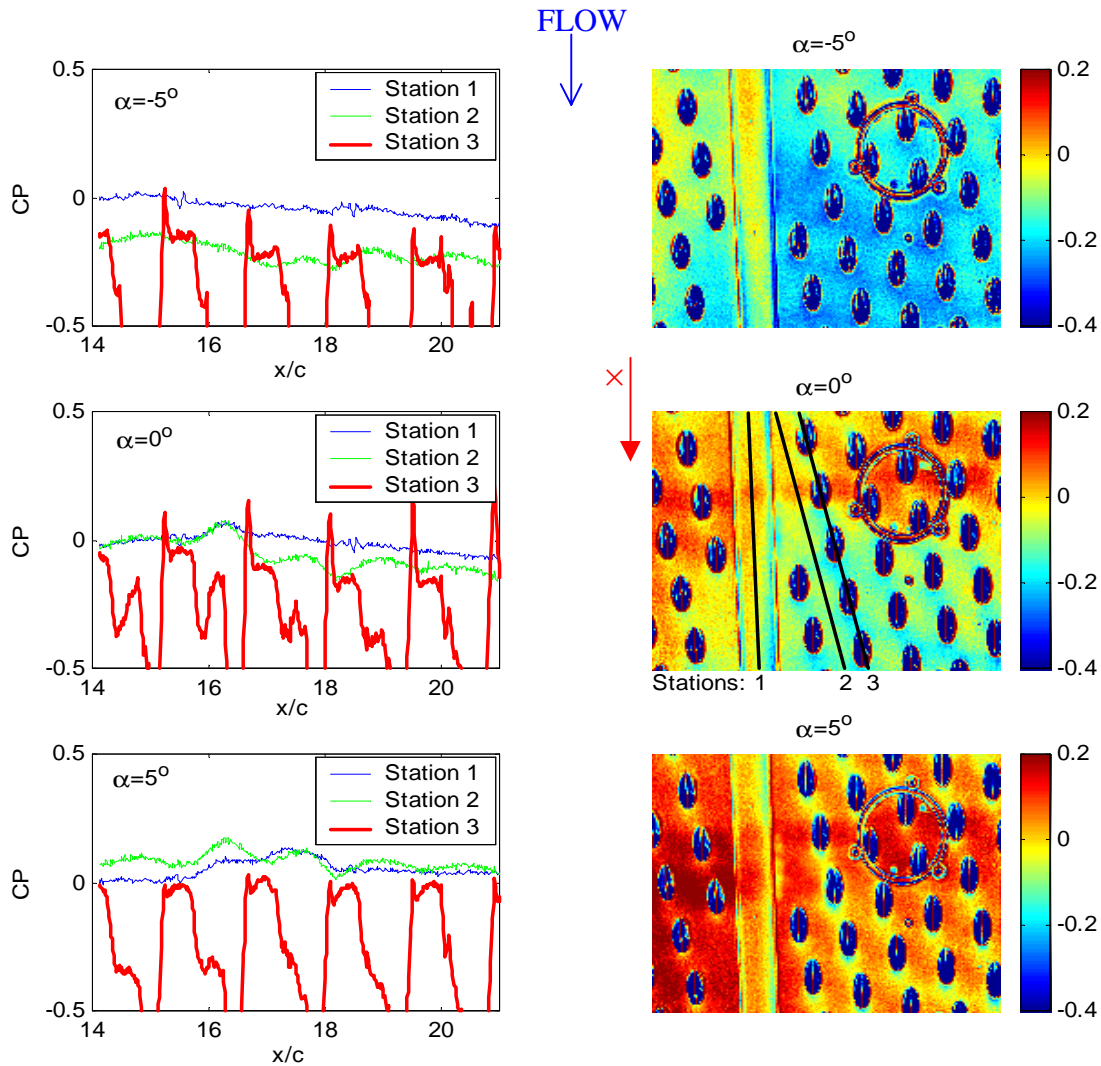
Fig.15 PSP measurements of 4%-open , 60°-slanted perforated walls, at $M_\infty=0.74$ and $Re=42\times10^6$.

Left : Cp profiles on the static-pressure tube (station 1) and two wall-survey lines (stations 2 and 3)

Right : surface Cp distributions of the patch, visualized in pseudo-colors.

6. Conclusions

The aim of this paper is to show that wind tunnel wall interference remains to be a challenging topic of applied aerodynamics. New research avenues in this largely non-linear discipline have been opened with modern computational and experimental techniques.

Acknowledgments

References

[1] Prandtl L. *Tragflügeltheorie*. Nachrichten der Gesellschaft der Wissenschaft zu Göttingen, Math.-Phys. Klasse, pp.107-137, 1919 (in German).

[2] Ewald B E (ed.). *Wind tunnel wall corrections*. AGARD-AG-336, pp.XIV-XV, 6.13-6.14, 12.7-12.8, 1998.

[3] Garner H C, Rogers E W E, Acum W E A, and Maskell E C. *Subsonic Wind Tunnel Wall Corrections.* AGARDograph 109, pp.319-321, 1966

[4] Mokry M. Automation of wall-interference procedures using the C++ object-oriented approach. AIAA 2000-0674, Reno, 2000.

[5] Ashill P R and Weeks D J. A method for determining wall-interference corrections in solid-wall tunnels from measurements of static pressure at the walls. AGARD-CP-335, pp.1.1 - 1.12, 1982.

[6] Ashill P R and Keating R F A. Calculation of tunnel wall interference from wall-pressure measurements. *The Aeronautical Journal of the Royal Aeronautical Society*, pp.36-53, 1988.

[7] Cooper K R, Corber A, and Stackhouse R An examination of wall-pressure-based correction methods with off-center models in a closed wind tunnel. National Research Council of Canada LTR-A-050, 2000.

[8] Hackett J E, Cooper K R, and Perry M L. Drag, lift and pitching moment increments due to wind tunnel wall constraint: extension to three dimensions. *ICAS 2000 Congress*, Harrogate, 2000.

[9] Ashill P R and Taylor C R, Mokry M, Cooper K R, and Hackett J E. Comments and replies on 'Tunnel-Induced gradients and their effect on drag'. *AIAA Journal*, Vol.36, pp.298-302, 1998.

[10] Emmons H W. Flow of a compressible fluid past a symmetrical airfoil in a wind tunnel and free air. NACA TN 1746. 1948.

[11] Dvořák R. *Transsonické proudění*. Academia, Prague, pp.13-19, 1986 (in Czech).

[12] Spreiter J R, Smith D W, and Hyett B J. A study of the simulation of flow with free-stream Mach number 1 in a choked wind tunnel. NASA TR R-73, 160, pp.771-778.

[13] Allen H J and Vincenti W G. Wall interference in a two-dimensional-flow wind tunnel, with consideration of the effect of compressibility. NACA 782, 1944.

[14] Mokry M. Finite volume solutions of two-dimensional Euler equations on adapted structured meshes. *Proc. CASI 1st Canadian Symposium on Aerodynamics.* Ottawa pp.15.1-15.13, 1989.

[15] Cooper G K and Sirbaugh J R. PARC code: theory and usage. Arnold Engineering Development Center, AEDC-TR-89-15, 1989.

[16] Khalid M and Mokry M. NPARC study of a transonic wall interference. *Journal of Aircraft*, Vol.33, pp.906-912, 1996.

[17] Shapiro, A H. *The dynamics and thermodynamics of compressible fluid flow*. Vol.1, pp. 260 and 544-548. J.Wiley, 1953.

[18] Collins D J and Krupp J A. Experimental and theoretical investigation in two-dimensional transonic flow. AIAA Journal, Vol.12, pp.771-778, 1974.

[19] Pope A and Goin K L. *High-speed wind tunnel testing*. J.Wiley, pp.305-307, 1965.

[20] Chew W L. Cross-flow calibration at transonic speeds of fourteen perforated plates with round holes and airflow parallel to the plates. AEDC-TR-54-65. 1955.

[21] Jacocks J L. Aerodynamic characteristics of perforated walls for transonic wind tunnels. Arnold Engineering Development Center, AEDC-TR-77-61, 1977.

[22] Mébarki Y. Pressure sensitive paint technique: from laboratory to wind tunnel. *ICAS 2000 Congress*, Harrogate, 2000.